

A deep primal-dual proximal network for image restoration

Mingyuan Jiu ^{*} Nelly Pustelnik [†]

December 21, 2021

Abstract

Image restoration remains a challenging task in image processing. Numerous methods tackle this problem, which is often solved by minimizing a nonsmooth penalized co-log-likelihood function. Although the solution is easily interpretable with theoretic guarantees, its estimation relies on an optimization process that can take time. Considering the research effort in deep learning for image classification and segmentation, this class of methods offers a serious alternative to perform image restoration but stays challenging to solve inverse problems. In this work, we design a deep network, named DeepPDNet, built from primal-dual proximal iterations associated with the minimization of a standard penalized co-log-likelihood with an analysis prior, allowing us to take advantage of both worlds.

We reformulate a specific instance of the Condat-Vũ primal-dual hybrid gradient (PDHG) algorithm as a deep network with fixed layers. Each layer corresponds to one iteration of the primal-dual algorithm. The learned parameters are both the PDHG algorithm step-sizes and the analysis linear operator involved in the penalization (including the regularization parameter). These parameters are allowed to vary from a layer to another one. Two different learning strategies: “Full learning” and “Partial learning” are proposed, the first one is the most efficient numerically while the second one relies on standard constraints ensuring convergence of the standard PDHG iterations. Moreover, global and local sparse analysis prior are studied to seek a better feature representation. We apply the proposed methods to image restoration on the MNIST and BSD68 datasets and to single image super-resolution on the BSD100 and SET14 datasets. Extensive results show that the proposed DeepPDNet demonstrates excellent performance on the MNIST dataset compared to other state-of-the-art

^{*}School of Information Engineering, Zhengzhou University, Zhengzhou, 450001, China. Email: iemyjiu@zzu.edu.cn

[†]Univ Lyon, Ens de Lyon, Univ Lyon 1, CNRS, Laboratoire de Physique, Lyon, 69342, France. Email: nelly.pustelnik@ens-lyon.fr

methods and better or at least comparable performance on the more complex BSD68, BSD100, and SET14 datasets for image restoration and single image super-resolution task.

1 Introduction

Inverse problem solving has been studied for many years with applications ranging from astrophysics to medical imaging. Among the numerous methods dedicated to this subject, we can first refer to the pioneering work by Tikhonov [1], studying the stability by introducing a smooth penalization, but also to the fundamental contributions about penalized co-log-likelihood by Geman and Geman [2] in the discrete setting and its continuous counterpart proposed by Mumford and Shah [3]. An important research effort was then related to compressed sensing theory, sparsity, and proximal algorithmic strategies, allowing to solve large size nonsmooth penalized co-log-likelihood objective function [4, 5]. Most of the contributions in inverse problems for image analysis between 2000 and 2015 were dedicated to such nonsmooth objective functions leading to major improvements in the reconstruction performance. In parallel, in the domain of image classification and segmentation, outstanding performances have been achieved using deep learning strategies [6], which offer a promising research direction for solving inverse problems too. However, its counterpart for inverse problems is still an active research area in order to obtain a solution as understandable and stable as the one obtained with the well-studied penalized co-log-likelihood minimization approaches.

In this work, we consider an original image $\bar{x} \in \mathbb{R}^N$ composed with N pixels and its degradation model:

$$z = A\bar{x} + \varepsilon \tag{1}$$

where $A \in \mathbb{R}^{M \times N}$ models a linear degradation, $\varepsilon \sim \mathcal{N}(0, \alpha^2 \mathbb{I})$ models the effect of white Gaussian noise with a standard deviation α , and $z \in \mathbb{R}^M$ denotes the observed data. The resolution of an inverse problem relies on the estimation of \hat{x} from the observations z , and possibly the knowledge of A . Penalized co-log-likelihood approaches rely on the minimization of an objective function being the sum of a data fidelity term (co-log-likelihood) and a penalization (prior), expressed in its most standard formulation as:

$$\hat{x}_\lambda \in \underset{x}{\text{Argmin}} \frac{1}{2} \|Ax - z\|_2^2 + \lambda p(Hx), \tag{2}$$

where $\lambda > 0$ denotes the regularization parameter allowing a tradeoff between the first term, insuring the solution to be *close to* the observations (and mostly designed according to the noise statistics), and the penalization involving a linear operator $H \in \mathbb{R}^{P \times N}$ and a function $p: \mathbb{R}^P \rightarrow]-\infty, +\infty]$. The modelization of the prior as the composition of a function with a linear operator allows us to model most of the standard penalization such as the smooth

convex Tikhonov or hyperbolic Total Variation penalization [7], the anisotropic or isotropic Total Variation (TV) [8, 9, 10, 11, 12, 13] or its generalization referred as non-local TV (NLTV) [14, 15], wavelet or frame based penalizations in its analysis formulation [16, 17], penalization based on Gaussian mixture models (GMM) such as EPLL [18], or BM3D for image denoising [19]. The reader can refer to [12, 20] for detailed overview and comparisons of these penalizations. The choice of the penalization is very dependent on the application due to the expected computational processing time and the structure of the data that can vary a lot from an application to another one.

A large panel of proximal-based algorithmic strategies have been developed to estimate \hat{x}_λ [4, 5, 21]. Among the most standard ones, we can refer to forward-backward (FB) algorithm [22] and related schemes as the iterative soft-thresholding algorithm (ISTA) and its accelerations [23, 24], Douglas-Rachford (DR) algorithm [25], ADMM or Split bregman iterations for which links have been established with DR [26], and more recently proximal primal-dual schemes (see [21] for a detailed review), especially PDHG [27, 28] providing a general algorithm that can be reduced to either FB or DR. In this work we propose to focus on this last mentioned primal-dual scheme [27] which appears flexible enough to solve (2) without requiring strong assumptions on A neither on H but only p to be convex, lower-semicontinuous and proper. The iterations of [27, 28] in the specific context of (2) are:

$$\begin{cases} \mathbf{x}^{[k+1]} &= \mathbf{x}^{[k]} - \tau A^*(A\mathbf{x}^{[k]} - \mathbf{z}) - \tau H^*\mathbf{y}^{[k]} \\ \mathbf{y}^{[k+1]} &= \text{prox}_{\sigma\lambda p^*}(\mathbf{y}^{[k]} + \sigma H(2\mathbf{x}^{[k+1]} - \mathbf{x}^{[k]})) \end{cases} \quad (3)$$

where prox denotes the proximity operator [4] and p^* is the conjugate function of p . Under technical assumptions, especially involving the choice of the step-sizes τ and σ , the sequence $(\mathbf{x}^{[k]})_{k \in \mathbb{N}}$ is insured to converge to \hat{x}_λ . For the challenging question of the selection of the optimal λ , one can either have recourse to supervised learning by selecting the optimal λ using a training database or to unsupervised technique such as the Stein Unbiased Risk Estimator (i.e. SURE), with successful applications in [29, 30]. It relies on

$$\underset{\lambda}{\text{minimize}} \mathbb{E}\{\|\phi(\hat{x}_\lambda - \bar{x})\|^2\},$$

and on a reformulation of this expression which does not involve the knowledge of ground-truth \bar{x} , leading either to the estimation risk when $\phi = \text{I}$ (can be handled in the context of inverse problems with full rank A) or a prediction risk that is $\phi = A$ (for more general linear degradation) [31, 32, 33, 34].

A recent alternative to variational formulation and nonsmooth optimization relies on supervised learning based on neural networks (see [35, 36] for review papers). The contributions dedicated to this subject are wide but the common point is to learn a prediction function f_Θ with a set of parameters Θ from a training data set $\mathcal{S} = \{(\bar{x}_s, z_s) | s = 1, \dots, I\}$

by minimizing an empirical loss function of the form:

$$E(\Theta) := \frac{1}{I} \sum_{s=1}^I \|f_{\Theta}(\ell_z(z_s)) - \ell_x(\bar{x}_s)\|^2.$$

The simplest approach consists of considering f_{Θ} as a CNN [37, 38, 39], leading to $\ell_z(z) = z$ and $\ell_x(x) = x$. Improved performance can be achieved when the learning is performed on wavelet or frame coefficients [40, 41, 42] (leading to ℓ_z and ℓ_x associated with the frame transform), and/or on backprojected data i.e. $\ell_z(z) = A^\dagger z$ (or also alternative relying on $\ell_z(z) = A^*z$) [43]. More recently, the design of f_{Θ} relies on the knowledge built for many years in inverse problems, for instance by truncated a Neumann series [44], or by unfolding iterative methods such as gradient descent scheme in [45], ISTA iterations as proposed in the pioneer work by Gregor and LeCun [46], proximal interior point iterations as in [47], and more recently by unfolding a proximal primal-dual optimization method [48] where proximal operators have been replaced with CNN (see also [49] for similar ideas). The last class of approaches, especially [47], offers a framework particularly suited for stability analysis [50].

Our contributions are first to reformulate a specific instance of the Condat-Vũ primal-dual hybrid gradient (PDHG) algorithm applied to solve (2) as a deep network with fixed layers. Each layer corresponds to one iteration of the primal-dual algorithm (Section 2). Based on this relation, a second contribution consists in reformulating primal-dual algorithm into a deep network framework aiming to learn both the algorithmic parameters σ , τ and also the regularization parameter λ and the linear operator H (as a unique entity λH) for a fixed number of layers K , leading to the proposed DeepPDNet (Section 3). Then, we design a backpropagation procedure based on an explicit differentiation with respect to the parameters of interest. Global and local sparse analysis prior are studied to seek better feature representation (Section 4). Finally, the proposed network is evaluated on image restoration and single image super-resolution problems with different levels of complexity in terms of noise, blur, and database (Section 5).

2 Neural networks versus Primal-dual proximal scheme

2.1 Condat-Vũ algorithm

The design of our neural network relies on a reformulation of (2), which is summarized in Problem 1.

Problem 1. *Let $A \in \mathbb{R}^{M \times N}$, $z \in \mathbb{R}^M$, $L \in \mathbb{R}^{P \times N}$, and g a convex, l.s.c, and proper function from \mathbb{R}^P to $] -\infty, +\infty]$ such that*

$$\hat{x}_{\lambda} \in \underset{x \in \mathbb{R}^N}{\text{Argmin}} \frac{1}{2} \|Ax - z\|_2^2 + g(Lx). \quad (4)$$

A particular instance of this problem is provided in (2) where $g \circ L = \lambda p(H \cdot)$. In the specific case where $p = \|\cdot\|_1$, then $L = \lambda H$, which allows us to combine the estimation of λ and H .

In order to solve the nonsmooth objective function (4) in a general setting without specific assumptions on L and A (e.g. a tight frame or a matrix associated with a filtering operation with periodic boundary effects), the most flexible and intelligible algorithm in the literature is certainly the Condat-Vũ algorithm [27], whose iterations specified to the resolution of Problem 1 are summarized in Algorithm 1.

Algorithm 1: Primal-dual splitting algorithm for solving Problem 1.

1 **Set:** $\tau > 0, \sigma > 0$, such that $\frac{1}{\tau} - \sigma\|L\|^2 > \frac{\|A\|^2}{2}$
2 **Initialization:** $(x^{[1]}, y^{[1]}) \in \mathcal{H} \times \mathcal{G}$
3 **for** $k = 1, \dots, K$ **do**
4 $x^{[k+1]} = x^{[k]} - \tau A^*(Ax^{[k]} - z) - \tau L^*y^{[k]}$
5 $y^{[k+1]} = \text{prox}_{\sigma g^*}(y^{[k]} + \sigma L(2x^{[k+1]} - x^{[k]}))$
6 **end**

The core ingredient of proximal algorithms is the proximal operator defined as:

$$(\forall x \in \mathcal{H}) \quad \text{prox}_g(x) = \arg \min_{y \in \mathcal{H}} \frac{1}{2}\|y - x\|_2^2 + g(y).$$

Several properties of the proximity operator have been established in the literature (see [4, 5] and reference therein). Among them, the Moreau identity allows us to provide a relation between a function g and its conjugate g^* : $\text{prox}_{\sigma g^*}(x) = x - \sigma \text{prox}_{g/\sigma}(x/\sigma)$ for some $\sigma > 0$.

The convergence of the sequence $(x^{[k+1]})_{k \in \mathbb{N}}$, generated by Algorithm 1, to a minimizer of (4) is ensured under a technical assumption involving the step-size parameters τ, σ , but also $\|A\|^2$ and $\|L\|^2$:

$$\frac{1}{\tau} - \sigma\|L\|^2 > \frac{\|A\|^2}{2}. \tag{5}$$

2.2 Deep Primal Dual Network

Deep networks are composed of a stack of layers. Each layer takes the output of the previous layer as input and obtains the feature maps after linear transforms (e.g. convolution) and nonlinear activation functions. Formally, a network with K layers can be written as

$$u^{[K]} = \eta^{[K]}(D^{[K]} \dots \eta^{[1]}(D^{[1]}u^{[1]} + b^{[1]}) \dots + b^{[K]}) \tag{6}$$

where, for every $k \in \{1, \dots, K\}$, $D^{[k]}$ is the weight matrix, $b^{[k]}$ is the bias, and $\eta^{[k]}$ is the nonlinear activation function. In the classical deep learning framework (e.g. CNNs), $D^{[k]}$

is regarded as the convolution operation with a collection of small filters and each filter is associated with a bias $b^{[k]}$, $\eta^{[k]}$ is a nonlinear activation function such as tanh, sigmoid or ReLU function, followed by a pooling layer (e.g max pooling, average pooling, etc.) that is acted to increase local receptive fields and to decrease the parameter number of the network as well.

Proposition 1 gives the iterations of Condat-Vũ primal-dual algorithm into the deep neural network formalism (6).

Proposition 1. *Algorithm 1 fits the network (6) when considering, for every $k \in \{1, \dots, K\}$, $D^{[k]} \in \mathbb{R}^{(N+P) \times (N+P)}$, $b^{[k]} \in \mathbb{R}^{N+P}$ and $\eta^{[k]}: \mathbb{R}^{N+P} \rightarrow \mathbb{R}^{N+P}$ such that*

$$\begin{cases} D^{[k]} = \begin{pmatrix} \text{Id} - \tau A^* A & -\tau L^* \\ \sigma L(\text{Id} - 2\tau A^* A) & \text{Id} - 2\tau \sigma L L^* \end{pmatrix} \\ b^{[k]} = \begin{pmatrix} \tau A^* z \\ 2\tau \sigma L A^* z \end{pmatrix} \\ \eta^{[k]} = \begin{pmatrix} \text{Id} \\ \text{prox}_{\sigma g^*} \end{pmatrix} \end{cases} \quad (7)$$

where Id denotes the identity matrix.

Proof. The result is straightforward setting

$$\mathbf{u}^{[k]} = \begin{pmatrix} \mathbf{x}^{[k]} \\ \mathbf{y}^{[k]} \end{pmatrix} \in \mathbb{R}^{N+P}$$

and from the rewriting of primal-dual updates as

$$\begin{cases} \mathbf{x}^{[k+1]} = (\text{Id} - \tau A^* A)\mathbf{x}^{[k]} - \tau L^* \mathbf{y}^{[k]} + \tau A^* z \\ \mathbf{y}^{[k+1]} = \text{prox}_{\sigma g^*}(\sigma L(\text{Id} - 2\tau A^* A)\mathbf{x}^{[k]} + \\ \quad (\text{Id} - 2\tau \sigma L L^*)\mathbf{y}^{[k]} + 2\tau \sigma L A^* z). \end{cases}$$

□

Proposition 1 presents how to unfold the specific instance of Condat-Vũ primal-dual algorithm described in Algorithm 1 into a network with multiple layers. This network performs unsupervised image restoration when the number of layers $K \rightarrow +\infty$ and it converges to the solution of Eq. (4). Practically, K needs to be set sufficiently large and its value is either set manually (e.g. $K > 10^5$) or based on a stopping criterion (e.g. based on residual of the iterates or on the duality gap).

When being reformulated into a supervised learning framework, an extremely large number of K becomes impractical and a deep network with a medium depth (e.g. ten or hundred layers), that could be interpreted as early stopping, would not provide such a good estimate. So we make several modifications in the network presented in Proposition 1 suited to a deep learning formalism.

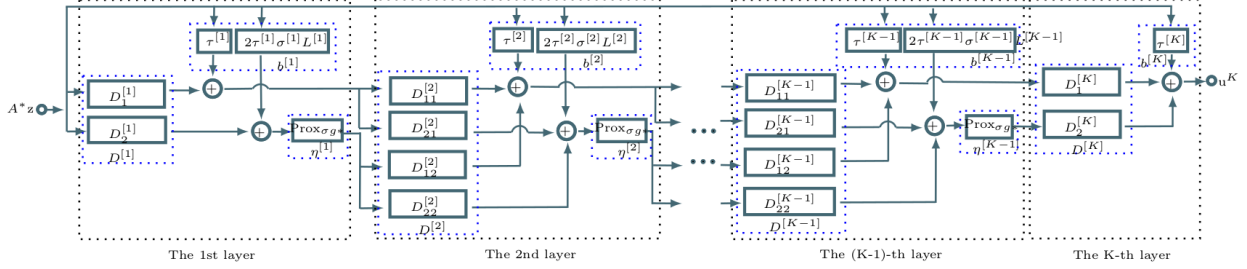


Figure 1: Illustration of the prediction function involved in the proposed DeepPDNet with K layers. In the figure, according to Eq. (9), $D_1^{[k]} = \text{Id} - \tau^{[k]}A^*A$, $k = 1, K$, $D_2^{[1]} = \sigma^{[1]}L^{[1]}(\text{Id} - 2\tau^{[1]}A^*A)$, $D_2^{[K]} = -\tau^{[K]}(L^{[K]})^*$, and for every $k = \{2, \dots, K-1\}$, $D_{11}^{[k]} = \text{Id} - \tau^{[k]}A^*A$, $D_{12}^{[k]} = -\tau^{[k]}(L^{[k]})^*$, $D_{21}^{[k]} = \sigma^{[k]}L^{[k]}(\text{Id} - 2\tau^{[k]}A^*A)$, $D_{22}^{[k]} = \text{Id} - 2\tau^{[k]}\sigma^{[k]}L^{[k]}(L^{[k]})^*$.

2.3 Choice of L

Given Problem 1, the linear operator L is regarded as a prior knowledge (e.g. horizontal/vertical finite-difference operator, frame transform, ...). Although the merit of the primal-dual splitting algorithm is capable of converging to a fix-point solution, two issues are worthy to be taken into account: on one hand, L is manually set according to prior knowledge, and it is not suitable for different types of datasets, and this may result to poor performance; on the other hand, for each new data, the inference of (4) will take many iterations to ensure the solution to be achieved, which may become impractical for large data.

In the next section, we deal with these two issues by reformulating the primal-dual algorithm into a deep network framework aiming to learn both the algorithmic parameters σ , τ , and also the linear operator L for a fixed number of layers K .

3 DeepPDNet : Deep primal dual network

3.1 Proposed supervised DeepPDNet

In a context of restoration where A is known, the degrees of freedom in the proposed network (cf. Proposition 1) may only come from σ , τ , L , and g .

In this work, the penalization g is fixed but we let freedom on L , including on its norm, leading to implicit freedom on the regularization parameter trade-off. The step-size parameters of the algorithm σ and τ are also learned. Additionally, it is assumed that the parameters may be different from a layer to another one, leading to $\Theta = \{\sigma^{[k]}, \tau^{[k]}, L^{[k]}\}_{1 \leq k \leq K}$.

Given the training set $\mathcal{S} = \{(\bar{x}_s, z_s) | s = 1, \dots, I\}$ where \bar{x}_s is the original image and z_s is its degraded counterpart following degradation model (1). The proposed supervised learning strategy, named DeepPDNet, allows us to learn the parameters $\hat{\Theta} = \{\hat{\sigma}^{[k]}, \hat{\tau}^{[k]}, \hat{L}^{[k]}\}_{1 \leq k \leq K}$ being a solution of:

$$\underset{\Theta}{\text{minimize}} E(\Theta) := \frac{1}{I} \sum_{s=1}^I \|\bar{x}_s - f_{\Theta}(z_s)\|_2^2 \quad (8)$$

where the prediction function is

$$f_{\Theta}(z_s) = \eta^{[K]}(D^{[K]}(\dots \eta^{[1]}(D^{[1]}u_s^{[1]} + b^{[1]}) \dots + b^{[K]})$$

with

$$\left\{ \begin{array}{l} u_s^{[1]} = A^*z_s \\ D^{[1]} = \begin{pmatrix} \text{Id} - \tau^{[1]}A^*A \\ \sigma^{[1]}L^{[1]}(\text{Id} - 2\tau^{[1]}A^*A) \end{pmatrix} \\ D^{[k]} = \begin{pmatrix} \text{Id} - \tau^{[k]}A^*A & -\tau^{[k]}(L^{[k]})^* \\ \sigma^{[k]}L^{[k]}(\text{Id} - 2\tau^{[k]}A^*A) & \text{Id} - 2\tau^{[k]}\sigma^{[k]}L^{[k]}(L^{[k]})^* \end{pmatrix} \\ b^{[k]} = \begin{pmatrix} \tau^{[k]}A^*z \\ 2\tau^{[k]}\sigma^{[k]}L^{[k]}A^*z_s \end{pmatrix} \\ \eta^{[k]} = \begin{pmatrix} \text{Id} \\ \text{prox}_{\sigma^{[k]}g^*} \end{pmatrix} \\ D^{[K]} = \begin{pmatrix} \text{Id} - \tau^{[K]}A^*A & \tau^{[K]}(L^{[K]})^* \end{pmatrix} \\ b^{[K]} = \tau^{[K]}A^*z_s \\ \eta^{[K]} = \text{Id}. \end{array} \right. \quad (9)$$

The learning function f_{Θ} is formed with layers which are a direct extension of the layers described in Proposition 1 where σ , τ , and L are replaced with parameters depending of the layer k i.e. $\sigma^{[k]}$, $\tau^{[k]}$, $L^{[k]}$. A specific attention needs to be paid due to the primal and dual input and output involved in the Condat-Vũ scheme. Indeed, the primal-dual algorithm outputs both a primal and a dual solution, while for the output of the network, we do not know the target solution for the dual variable, then we cannot handle the dual solution in the objective function. Thus, if a standard choice for the primal and dual variables setting is $x^{[1]} = A^*z_s$ and $y^{[1]} = LA^*z_s$, in order to fit (8), the initialization of the dual variable is set to $y^{[1]} = 0$. The last layer also needs to be modified in order to only extract the primal variable.

3.2 Backpropagation procedure

The most standard strategy to estimate the parameters in a neural network relies on a stochastic gradient descent algorithm where the objective function is $E(\Theta)$ defined in (8).

The increments of the parameters are computed from the data (mini-batch strategy is adopted in practice) after forwarding the data through the network. The increments at iteration $\ell + 1$ consist of

$$\Theta_{[\ell+1]} = \Theta_{[\ell]} - \gamma \nabla E(\Theta_{[\ell]}),$$

relying on the updates of each parameter, for every $k \in \{1, \dots, K\}$,

$$\begin{cases} \tau_{[\ell+1]}^{[k]} &= \tau_{[\ell]}^{[k]} - \gamma \frac{\partial E}{\partial \tau_{[\ell]}^{[k]}} \\ \sigma_{[\ell+1]}^{[k]} &= \sigma_{[\ell]}^{[k]} - \gamma \frac{\partial E}{\partial \sigma_{[\ell]}^{[k]}} \\ L_{[\ell+1]}^{[k]} &= L_{[\ell]}^{[k]} - \gamma \frac{\partial E}{\partial L_{[\ell]}^{[k]}} \end{cases} \quad (10)$$

where $\gamma > 0$ is learning step. In order to obtain the gradients in the different layers, we employ a backpropagation procedure, i.e. the errors are backpropagated from last layer to the first layer.

To make clear the presentation of the estimation of Θ , we first rewrite the network feedforward procedure from the layer k to layer $k + 1$ as follows:

$$\mathbf{c}_s^{[k]} = D^{[k]} \mathbf{u}_s^{[k]} + b^{[k]} \quad (11)$$

$$\mathbf{u}_s^{[k+1]} = \eta^{[k]}(\mathbf{c}_s^{[k]}). \quad (12)$$

For input data z_s , the forward procedure to obtain $\mathbf{u}_s^{[K]} = f_{\Theta}(z_s)$ of the network is described in Algorithm 2.

Algorithm 2: Forward procedure

Input: Set $D^{[k]}, b^{[k]}, \eta^{[k]}, k = \{1, \dots, K\}$ according to (9).

Data: Set $\mathbf{u}_s^{[1]} = A^* z_s, s = \{1, \dots, I\}$

- 1 **for** $k = 1, \dots, K$ **do**
 - 2 Perform linear transformation by Eq. (11): $\mathbf{c}_s^{[k]} = D^{[k]} \mathbf{u}_s^{[k]} + b^{[k]}$;
 - 3 Perform nonlinear activation function by Eq. (12): $\mathbf{u}_s^{[k+1]} = \eta^{[k]}(\mathbf{c}_s^{[k]})$;
 - 4 **end**
-

Since $\tau^{[k]}, \sigma^{[k]}$, and $L^{[k]}$ are jointly involved in $D^{[k]}, b^{[k]}$ and $\eta^{[k]}$, so their gradients at iteration ℓ read:

$$\frac{\partial E}{\partial \tau_{[\ell]}^{[k]}} = \frac{\partial E}{\partial b_{[\ell]}^{[k]}} \frac{\partial b_{[\ell]}^{[k]}}{\partial \tau_{[\ell]}^{[k]}} + \frac{\partial E}{\partial D_{[\ell]}^{[k]}} \frac{\partial D_{[\ell]}^{[k]}}{\partial \tau_{[\ell]}^{[k]}} \quad (13)$$

$$\frac{\partial E}{\partial \sigma_{[\ell]}^{[k]}} = \frac{\partial E}{\partial \mathbf{u}_s^{[k+1]}} \frac{\partial \mathbf{u}_s^{[k+1]}}{\partial \sigma_{[\ell]}^{[k]}} + \frac{\partial E}{\partial b_{[\ell]}^{[k]}} \frac{\partial b_{[\ell]}^{[k]}}{\partial \sigma_{[\ell]}^{[k]}} + \frac{\partial E}{\partial D_{[\ell]}^{[k]}} \frac{\partial D_{[\ell]}^{[k]}}{\partial \sigma_{[\ell]}^{[k]}} \quad (14)$$

$$\frac{\partial E}{\partial L_{[\ell]}^{[k]}} = \frac{\partial E}{\partial b_{[\ell]}^{[k]}} \frac{\partial b_{[\ell]}^{[k]}}{\partial L_{[\ell]}^{[k]}} + \frac{\partial E}{\partial D_{[\ell]}^{[k]}} \frac{\partial D_{[\ell]}^{[k]}}{\partial L_{[\ell]}^{[k]}} \quad (15)$$

where the gradients of E w.r.t. $D_{[\ell]}^{[k]}$ and $b_{[\ell]}^{[k]}$ are then computed as:

$$\frac{\partial E}{\partial D_{[\ell]}^{[k]}} = \frac{\partial E}{\partial \mathbf{c}_s^{[k]}} \frac{\partial \mathbf{c}_s^{[k]}}{\partial D_{[\ell]}^{[k]}} = \frac{\partial E}{\partial \mathbf{c}_s^{[k]}} (\mathbf{u}_s^{[k]})^\top \quad (16)$$

$$\frac{\partial E}{\partial b_{[\ell]}^{[k]}} = \frac{\partial E}{\partial \mathbf{c}_s^{[k]}}. \quad (17)$$

and where the errors for the variable $\mathbf{c}_s^{[k]}$ and $\mathbf{u}_s^{[k]}$ at layer $[k]$ are obtained according to Eq. (12) and Eq. (11) by chain rule:

$$\frac{\partial E}{\partial \mathbf{c}_s^{[k]}} = \frac{\partial E}{\partial \mathbf{u}_s^{[k+1]}} \frac{\partial \mathbf{u}_s^{[k+1]}}{\partial \mathbf{c}_s^{[k]}} \quad (18)$$

$$\frac{\partial E}{\partial \mathbf{u}_s^{[k]}} = D_{[\ell]}^{[k]} \frac{\partial E}{\partial \mathbf{c}_s^{[k]}}, \quad (19)$$

relying on the error of loss E w.r.t. $\mathbf{u}_s^{[k+1]}$ at the layer $k+1$ (denoted as $\frac{\partial E}{\partial \mathbf{u}_s^{[k+1]}}$) that is already known starting from the error of loss E w.r.t. $\mathbf{u}_s^{[K]}$:

$$\frac{\partial E}{\partial \mathbf{u}_s^{[K]}} = \frac{2}{I} (\mathbf{u}_s^{[K]} - \bar{\mathbf{x}}_s). \quad (20)$$

The expression of the gradients are provided in Appendix A. The backward procedure is detailed in Algorithm 3.

3.3 Full versus Partial learning

We propose two versions of our network: Full DeepPDNet and Partial DeepPDNet. Full DeepPDNet denotes the proposed supervised strategy described in Section 3.1 relying on

Algorithm 3: Backward procedure of “Full learning”

Input: Set $D^{[k]}, b^{[k]}, \eta^{[k]}, k = \{1, \dots, K\}$ according to (9) and set $\gamma > 0$
Data: Set $u_s^{[1]} = A^*z_s$ for every $s = \{1, \dots, I\}$

- 1 **for** $\ell = 1, \dots, T$ **do**
- 2 Select one training sample $u_s^{[1]}$, calculate the gradient of loss w.r.t. $u_s^{[K]} = f_{\Theta_{[\ell]}}(u_s^{[1]})$ according to Eq. (20);
- 3 **for** $k = K - 1, \dots, 1$ **do**
- 4 Backpropagate the errors to $c_s^{[k]}$ and $u_s^{[k]}$ in the $[k]$ layer according to Eq. (18) and (19);
- 5 **end**
- 6 **for** $k = K, \dots, 1$ **do**
- 7 Calculate the gradients of the loss w.r.t. $D^{[k]}$ and $b^{[k]}$ according to Eq. (16) and (17);
- 8 Calculate the gradients of the loss w.r.t. $\tau^{[k]}, \sigma^{[k]}$ and $L^{[k]}$ according to Eq. (13), (14) and (15).
- 9 **end**
- 10 Update $\tau_{[\ell+1]}^{[k]}, \sigma_{[\ell+1]}^{[k]}$ and $L_{[\ell+1]}^{[k]}$ for layers $k \in \{1, \dots, K\}$ by Eq. (10).
- 11 **end**

the learning of $\tau^{[k]}, L^{[k]}$, and $\sigma^{[k]}$. Partial DeepPDNet is reduced to the learning of $\tau^{[k]}$ and $L^{[k]}$ while $\sigma^{[k]}$ is set as:

$$\sigma^{[k]} = \frac{1/\tau^{[k]} - \|A\|^2/2}{\|L^{[k]}\|^2}. \quad (21)$$

This choice is guided by the technical assumptions insuring the convergence of the sequence $(x^{[k]})_{k \in \mathbb{N}}$, generated by standard Condat-Vũ algorithm (cf. Algorithm 1), to \widehat{x}_λ defined in (4). In the experimental section, we investigate the performance for both learning strategies (cf. Section 5).

4 Global vs local structured L

The penalization term $g(Lx)$ in Eq. (4) can be considered as prior enforcing some smoothness on the solution. In many references of the recent inverse problem literature, g denotes a ℓ_1 -norm or a $\ell_{1,2}$ -norm in order to obtain sparse features. In the scenario of image restoration, L usually models the discrete horizontal and vertical difference or other linear operator allowing to capture discontinuities. From other published research, it is well known that the structure of L has a crucial impact on the performance of image restoration.

In the proposed DeepPDNet, each layer $k \in \{1, \dots, K\}$ involves a learned linear transform $L^{[k]} \in \mathbb{R}^{P \times N}$, where each row corresponds to a learned pattern of the image. In

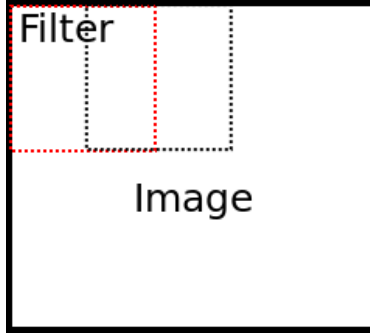


Figure 2: Sliding window modelling the location of the non-zero coefficients for each row of $L^{[k]}$ in the *local features* setting.

this work, we study three architectures for $L^{[k]}$: (i) $L^{[k]}$ is a dense matrix, (ii) $L^{[k]}$ is a block-sparse matrix, (iii) $L^{[k]}$ is built as a combination of dense and block-sparse matrices, respectively describing the global, the local, and the mixed global-local patterns. More specifically,

- Global patterns: $L^{[k]}$ is built without any prior knowledge. It is a dense matrix from the image space \mathbb{R}^N to a feature space \mathbb{R}^P . Each row attempts to learn one type of global structure that occur in the image. In practice, $L^{[k]}$ is initialized by random values following a normal distribution.
- Local patterns: we construct a matrix $L^{[k]}$ with local sparse structures, which is inspired by the local patch dictionary [51]. For each row of $L^{[k]}$, $Q \times Q$ non-zero coefficients are locating in the region illustrated in Fig. 2. The location of the window, and thus of the non-zero coefficients, is slided through the image. In our experiments, the values of the non-zero coefficients are randomly initialized according to a normal distribution. In the learning procedure, the non-zeros elements in $L^{[k]}$ are updated, the other ones remain zero.
- Mixed global-local patterns: $L^{[k]}$ is built as a combination of dense and block-sparse matrices.

Global and local $L^{[k]}$ are respectively related to the fully connected layer and the convolution layer, but they are not the same. Indeed, if we consider a network with K layers formally defined as in (6), the fully connected layer or convolutional layer are implemented in $(D^{[k]})_{1 \leq k \leq K}$ as being either a dense matrix or a block-sparse matrix, while in our network, $D^{[k]}$ has a special structure coming from Condat-Vũ proximal iterations, whose expression is given in Section 3.1 as:

$$D^{[k]} = \begin{pmatrix} \text{Id} - \tau^{[k]} A^* A & -\tau^{[k]} (L^{[k]})^* \\ \sigma^{[k]} L^{[k]} (\text{Id} - 2\tau^{[k]} A^* A) & \text{Id} - 2\tau^{[k]} \sigma^{[k]} L^{[k]} (L^{[k]})^* \end{pmatrix}.$$

In this work, we consider similarly either dense matrix or block-sparse matrix but at the level of the analysis operator $L^{[k]}$.

Among the three configurations listed above (global, local-sparse, and mixed global-local), the combination of mixed global-local is the closest from recent CNNs, where fully connected layers and convolutional layers are combined in a cascade way. The numerical impact of these different choices for $L^{[k]}$ will be discussed in the next section.

5 Experiments

5.1 Network

A deep primal dual network with K layers has been built according to Section 3 with $g = \|\cdot\|_1$ and the weights in each layer are initialized by Eq. (9) such that $\tau^{[k]} \equiv 1$, $L^{[k]} \in \mathbb{R}^{P \times N}$ (where N is the raw image dimensionality and P denotes the embedded feature number) is randomly initialized by values following a normal distribution with a standard deviation set to 10^{-2} , and $\sigma^{[k]} = \frac{(1/\tau^{[k]} - \|A\|^2/2)}{\|L^{[k]}\|^2}$.

5.2 Dataset

We consider a training set $\mathcal{S} = \{(\bar{x}_s, z_s) | s = 1, \dots, I\}$ and an evaluation set $\mathcal{T} = \{(\bar{x}_s, z_s) | s = 1, \dots, J\}$ respectively containing I images and J images, where \bar{x}_s is the original image and z_s is its degraded counterpart obtained by the degradation model (1).

Two different inverse problems are considered: image restoration and single image super-resolution. In image restoration experiments, A models a uniform blur and the noise is a white Gaussian noise with variance α^2 . The size of the blur and the variance are specified for each experiment. For single image super-resolution, A denotes a decimation operator and no noise is considered.

We evaluate the performance of the proposed network in the context of image restoration on MNIST dataset [52] and BSD68 dataset [53] and in the context of super-resolution on BSD100 dataset [54] and SET14 [55] datasets used in [56].

5.3 Performance evaluation

The restoration performance are evaluated in terms of PSNR (i.e. Peak Signal-to-Noise Ratio) and SSIM (i.e. Structural SIMilarity), where higher values stand for better performance.

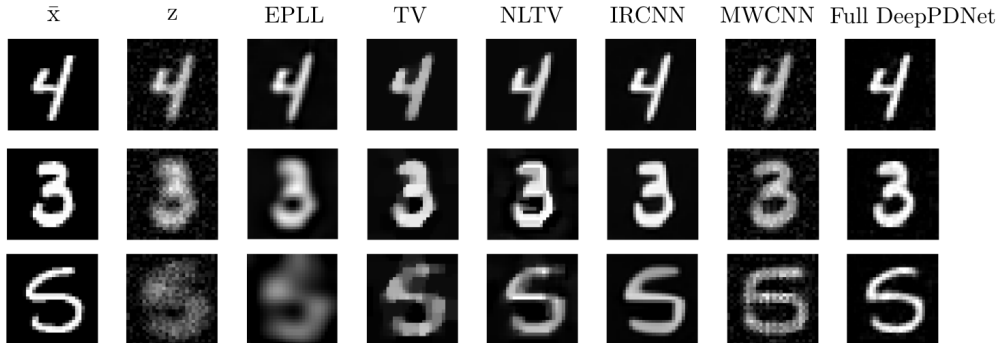


Figure 3: Visual comparisons on MNIST dataset for different methods. The first row corresponds to the MNIST data with a uniform 3×3 blur and a Gaussian noise with $\alpha = 20$, the second row is with a uniform 5×5 blur and a Gaussian noise with $\alpha = 20$, the third row is with a uniform 7×7 blur and a Gaussian noise with $\alpha = 20$. For each instance, the images from the first to the seventh column respectively correspond to the original one \bar{x} , the degraded one z , the restored ones by EPLL, TV, NLTV, IRCNN and the proposed full DeepPDNet ($K = 6$).

The convergence of the primal-dual scheme on which relies the deep learning procedure is insured when condition (5) is satisfied. To estimate the distance to this constraint we compute:

$$d_C(\tau^{[k]}, \sigma^{[k]}, L^{[k]}) = \max \left(0, \frac{\|A\|^2}{2} - \frac{1}{\tau^{[k]}} + \sigma^{[k]} \|L^{[k]}\|^2 \right)^2 \quad (22)$$

The simulations have been performed by a workstation with 4 cores and each is 3.20GHz (Intel Xeon(R) W-2104 CPU) and 64G memory. The code is implemented in MATLAB.

5.4 Performance on MNIST dataset

The MNIST dataset is a widely used handwritten benchmark for classification, containing 60,000 training images and 10,000 test images and each has a dimensionality of 28×28 . Instead of a classification task, in this work, it is used for image restoration. In the training procedure, the training set is further split into two subsets: 50,000 for training and the rest for validation. A hold-out validation scheme is applied to estimate the network architecture.

The instances of clean images and their respective degraded ones are shown in Fig. 3. In the following experiments, we adopt a mini-batch stochastic gradient descent algorithm to update the parameters with a batch size of 200 for the network learning. The maximum iteration is set to 3×10^4 .

Impact of network depth (i.e. K) – To study the impact of the architecture depth of the

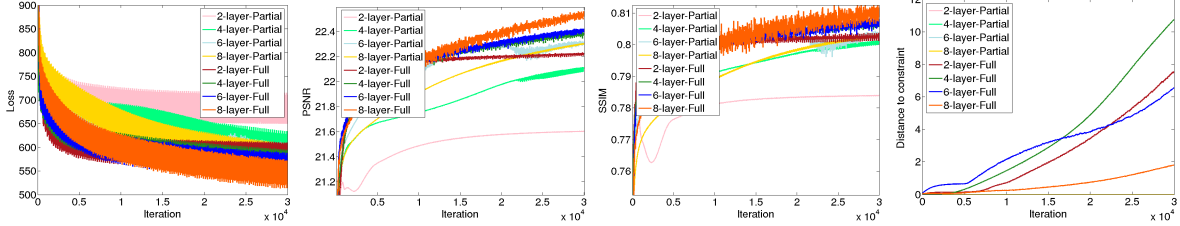


Figure 4: From left to right: Training loss, performance in terms of PSNR and SSIM on the validation set of MNIST dataset set, and d_C defined in (22) for full and partial learning with 2-layer, 4-layer, 6-layer and 8-layer networks and $P = 100$. The results are obtained from data degraded with a uniform 3×3 blur and a Gaussian noise with $\alpha = 20$. (Best visualisation in color)

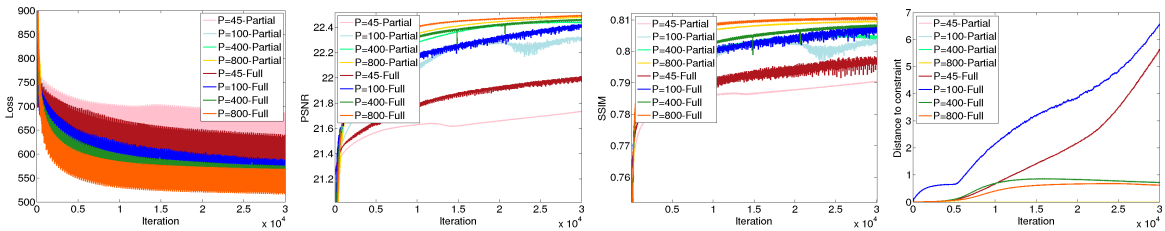


Figure 5: From left to right: Training loss, performance in terms of PSNR and SSIM on the validation set of MNIST dataset set, and d_C defined in (22) for full and partial learning with 6-layer and $P = 25, 100, 400, 800$. The results are obtained from data degraded with a uniform 3×3 blur and a Gaussian noise with $\alpha = 20$. (Best visualisation in color)

network, we conduct the experiments for Partial DeepPDNet and Full DeepPDNet described in Section 3.3 on 2-layer, 4-layer, 6-layer, and 8-layer networks with a fixed embedded feature number $P = 100$ and with global $L^{[k]}$. The simulations are performed with a uniform 3×3 blur and an additive Gaussian noise with a standard deviation $\alpha = 20$. The training loss, PSNR, SSIM, and the distance to convex constraint in the last layer w.r.t. the iterations on the validation set are displayed in Fig. 4. It can be seen that: i) Full DeepPDNet gives better results than Partial DeepPDNet; ii) Deeper architecture generally produces better results due to more meaningful feature learning; iii) the 8-layer network obtains a marginal gain compared to its 6-layer counterpart. The average cost time for one iteration of one mini-batch learning (including forward and backward process) is presented in Tab. 2 for different configurations of Full DeepPDNet. In our simulations, we perform training considering 30,000 iterations, which leads to a learning time going from 2 hours to 13 hours depending on the number of layers. Combining the computation cost and that marginal benefit with the 8-layer network, we adopt the architecture of a 6-layer network in the following experiments.

Impact of the size of $L^{[k]}$ (i.e. P) – For the 6-layer network, we study the impact of the size of P (i.e. $P = 25, 100, 400, 800$) in the scenario of Partial DeepPDNet and Full

Setting	“f28s28n10”	“f14s14n10”	“f14s7n10”	“f9s9n10”	“f9s4n10”	“f7s7n10”	“f7s3n10”	“f5s5n10”	“f5s2n10”	“f3s3n10”
P	10	40	90	90	160	160	640	250	1210	810
Sparsity rate	0%	75%	75%	89.67%	89.67%	93.75%	93.75%	96.81%	96.81%	98.85%

Table 1: Value of P and sparsity rate for different choices of local sparse $L^{[k]}$. The smaller is the sparsity rate, the denser is $L^{[k]}$.

DeepPDNet described in Section 3.3 with global $L^{[k]}$. The simulations are performed with a uniform 3×3 blur and an additive Gaussian noise with a standard deviation $\alpha = 20$. The results are displayed in Fig. 5. It can be seen that: i) Full DeepPDNet leads to better performance than Partial DeepPDNet for similar P ; ii) Larger P leads to better results due to more feature embedding. However, when $P = 800$, the performance is close to the ones with $P = 400$, which demonstrates that when P becomes large, the capacity of improvement becomes limited.

Full versus Partial learning – From the above results, we can observe that the learning capacity is boosted when the feasible parameter space is enlarged (cf. with Full DeepPDNet), leading to a better solution than with Partial DeepPDNet.

The difference between Partial DeepPDNet and Full DeepPDNet only relies on the estimation of K additional parameters $(\sigma^{[k]})_{1 \leq k \leq K}$, which is small compared to the $K \times (PN + 1)$ parameters due to the learning of $(L^{[k]}, \tau^{[k]})_{1 \leq k \leq K}$ in the context of dense matrices or even compared to the $K \times (PQ^2 + 1)$ when block-sparse matrices are involved. This is certainly the reason why we do not observe overfitting. Indeed, from the results displayed in Fig. 4 and Fig. 5, we can observe that, for each configuration, the training loss decreases as a function of the iterations while the PSNR and SSIM on the validation set increases w.r.t. the iterations and does not imply performance drop. This quantitative results illustrate that no overfitting appears either with or without additional learned parameter $\sigma^{[k]}$.

Architecture	Time (s)
2-layer	0.3460
4-layer	0.8368
6-layer	1.2767
8-layer	1.6084

Table 2: Average cost time (in s) for one learning iteration (including forward and backward) of one mini-batch of MNIST dataset for different network configurations.

Distance to the constraint – Here, we investigate the distance to the convex set for the full learning in two different viewpoints: the distance for different depths and also different P in the last layer of the networks. The distances to the constraint (22) w.r.t. the iterations for different depth and different P are shown in the last column of Fig. 4 and Fig. 5 respectively. It can be seen that the distance in the last layer decreases as the network becomes deep and also as P value becomes large, which reflects the learning ability of a large network. From these results, although full learning relaxes the constraint between the parameters, it

P	PSNR		SSIM	
	Global	Local sparse	Global	Local sparse
10	21.64	21.61	0.7846	0.7831
40	22.23	22.22	0.8033	0.8041
90	22.35	23.06	0.8052	0.8287
160	22.35	23.06	0.8052	0.8370
250	22.40	22.72	0.8059	0.8466
640	22.49	24.48	0.8076	0.9122
810	22.50	24.37	0.8113	0.9202
1210	22.49	24.80	0.8112	0.9278

Table 3: Comparison results of global and local $L^{[k]}$ according to Tab. 1 on the validation set of MNIST dataset from data degraded by a uniform 3×3 blur and a Gaussian noise with $\alpha = 20$. $P = 90$ corresponds to the setting of “f14s7n10” showing better performance than “f9s9n10” and $p = 160$ corresponds to the setting of “f7s7n10”.

Fusion	P	PSNR/SSIM
“f5s2n10”	1210	24.80/0.9278
“f5s2n10” + “f7s3n10”	1850	25.04/0.9317
“f5s2n10” + “f7s3n10” + “f14s7n10”	1940	25.06/0.9301
“f5s2n10” + “f7s3n10” + “f14s7n10” + “f28s28n10”	1950	25.33/0.9335

Table 4: Performance of combination of multiple local sparse filters on the validation MNIST dataset with uniform blur filter 3×3 and Gaussian noise $\alpha = 20$.

has the ability to make the violation distance smaller when making the network deeper or larger. Obviously, the constraint is always satisfied with Partial learning.

Local vs global matrix – Next, we investigate the performance of dense matrix (global) and block-sparse matrix (local) described in Section 4. We consider ten types of local sparse projection in L for the 6-layer network: “f28s28n10”, “f14s14n10”, “f14s7n10”, “f9s9n10”, “f9s4n10”, “f7s7n10”, “f7s3n10”, “f5s5n10”, “f5s2n10” and “f3s3n10”, which is named as the format of “fQsNnS” such that “Q” stands for the size of local square filter, “N” means the strip length between two neighboring filters and “S” means the number of filters at the same location. The corresponding P number for each type is respectively shown in Tab. 1, at the same time, we also give the sparsity rate of L . It is noted that local filter “f28s28n10” with $P = 10$ corresponds to a dense matrix. To provide fair comparisons of the performance between global projection and local sparse projection, for each type of local sparse projection, we create a global projection with the same value for P . Their performance on the validation set is shown in Tab. 3. From the results, it is seen that: i) when P becomes larger, the performance of global projection slightly increase and remain stable when $P = 810$; ii) The performance of local sparse projection obtain significant improvement compared to global projection when the same P is adopted, especially for

Data	Method	3 × 3 Blur			5 × 5 Blur	7 × 7 Blur
		$\alpha = 10$	$\alpha = 20$	$\alpha = 30$	$\alpha = 20$	$\alpha = 20$
		PSNR/SSIM	PSNR/SSIM	PSNR/SSIM	PSNR/SSIM	PSNR/SSIM
MNIST	EPLL [18]	24.02/0.8564	20.99/0.7628	19.05/0.6871	16.42/0.5629	13.97/0.3265
	TV [8]	25.07/0.8583	19.58/0.7004	18.86/0.6681	18.86/0.6681	16.31/0.5665
	NLTV [57]	25.49/0.8697	21.98/0.7738	20.73/0.7353	20.73/0.7353	16.79/0.6228
	MWCNN [58]	19.16/0.7219	18.53/0.6782	17.78/0.6499	15.83/0.5343	13.04/0.3175
	IRCNN [59]	28.52 /0.8904	25.00/0.8193	22.63/0.7723	21.46/0.7698	18.29/0.6546
	Partial DeepPDNet	23.67/0.8366	22.03/0.7983	20.93/0.7750	17.96/0.6534	16.21/0.5505
	Full DeepPDNet	27.40/ 0.9410	25.09/0.9254	23.61/0.9097	22.43/0.8738	20.43/0.8157

Table 5: Comparison results of different methods on the MNIST dataset from different degradation configurations.

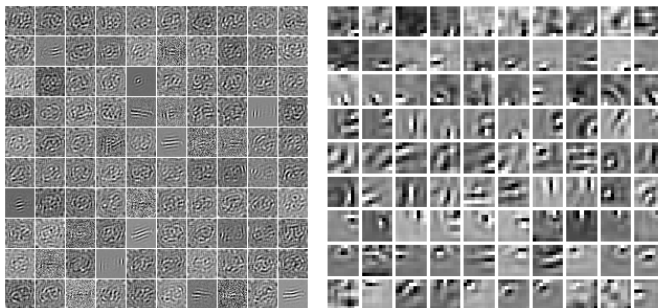


Figure 6: Visualization of the rows of $L^{[k]}$ for the layer $k = 6$ when considering Full DeepPDNet in the context of data degraded by a uniform 3×3 blur and an additive Gaussian noise with $\alpha = 20$ on MNIST dataset. (a) Global patterns when $P = 100$: each image is associated with a reshaped row of $L^{[6]}$ leading to 100 small images of size $\sqrt{N} \times \sqrt{N}$. (b) Reshaped rows of the block-sparse $L^{[6]}$ for the setting “f9s9n10” when $Q = 9$, $P = 90$ leading to 90 small filters of size 9×9 .

Data	Noise	Method	3 × 3 Blur		5 × 5 Blur		7 × 7 Blur	
			$\alpha = 20$		$\alpha = 20$		$\alpha = 20$	
			PSNR/SSIM	Relative Drop	PSNR/SSIM	Relative Drop	PSNR/SSIM	Relative Drop
MNIST	$\beta = 2$	MWCNN	18.52/0.6763	0.05/0.28	15.83/0.5340	0/0.06	13.04/0.3175	0/0
		IRCNN	24.84/0.8149	0.64/0.54	21.39/0.7654	0.33/0.57	18.24/0.6501	0.27/0.69
		Full DeepPDNet	25.05/0.9226	0.16/0.30	22.40/0.8709	0.13/0.33	20.40/0.8127	0.15/0.37
	$\beta = 5$	MWCNN	18.46/0.6722	0.38/0.88	15.80/0.5320	0.19/0.43	13.01/0.3158	0.23/0.54
		IRCNN	24.61/0.8079	1.56/1.39	21.24/0.7584	1.03/1.48	18.14/0.6428	0.82/1.80
		Full DeepPDNet	24.90/0.9159	0.76/1.03	22.29/0.8640	0.62/1.12	20.29/0.8051	0.69/1.30
	$\beta = 10$	MWCNN	18.26/0.6639	1.46/2.11	15.67/0.5257	1.01/1.61	12.85/0.3068	1.46/3.37
		IRCNN	24.04/0.7958	3.84/2.87	20.89/0.7459	2.66/3.10	17.90/0.6294	2.13/3.85
		Full DeepPDNet	24.45/0.8994	2.55/2.81	21.95/0.8465	2.14/3.12	19.93/0.7852	2.45/3.74
	$\beta = 20$	MWCNN	17.56/0.6433	5.23/5.15	15.07/0.4968	4.80/7.02	12.22/0.2688	6.29/15.34
		IRCNN	22.51/0.7693	9.96/6.10	19.84/0.7157	7.55/7.03	17.17/0.5966	6.12/8.86
		Full DeepPDNet	22.99/0.8547	8.37/7.67	20.77/0.7954	7.40/8.97	18.70/0.7224	8.47/11.44

Table 6: Comparisons of PSNR, SSIM and relative drops (in %) on the test MNIST dataset degraded with noise to evaluate the robustness when considering MWCNN, IRCNN and the proposed “Full DeepPDNet”.

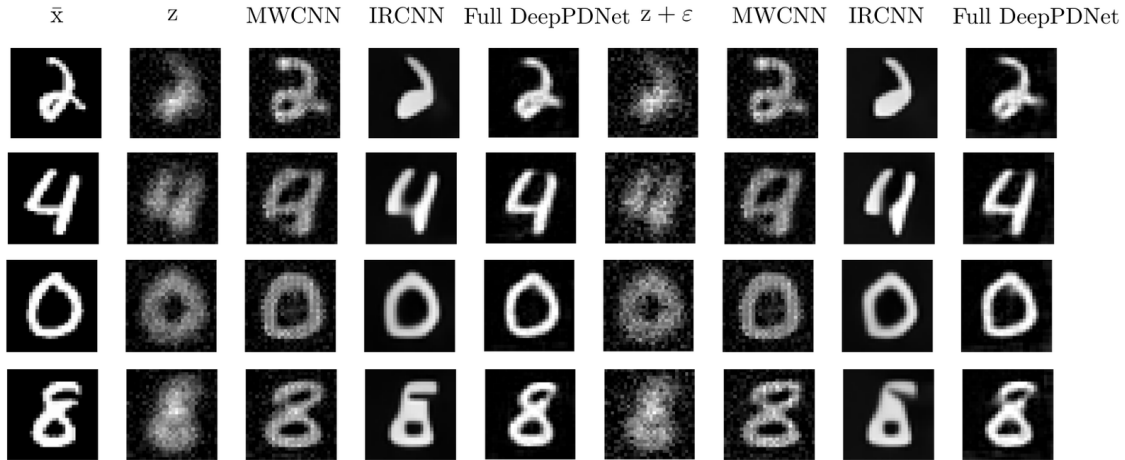


Figure 7: Visual comparisons of robustness analysis on the MNIST dataset with a uniform 7×7 blur and a Gaussian noise with $\alpha = 20$. From the first row to fourth row, the addition noises are $\beta = 2$, $\beta = 5$, $\beta = 10$ and $\beta = 20$. For each row, the images are the clean image, the blur image, the result by MWCNN, the result by IRCNN, the result by the learned full DeepPDNet ($K = 6$), the blur image with additional noise and its result by MWCNN, IRCNN, and the learned full DeepPDNet ($K = 6$).

large P ; iii) The performance of global matrix converges earlier than local sparse projection as P increases.

Fusion of multiple block-sparse matrices: Previously, we observe that block-sparse (i.e. local) $L^{[k]}$ has better performance than dense (i.e. global) ones. Since the block-sparse configuration is able to learn meaningful local patterns (as shown in Fig. 6), then we propose to investigate the performance of the fusion of multiple of block-sparse matrices. The performance of a combination of block-sparse matrices on the validation set is shown in Tab. 4. We can conclude that the performance is further boosted when multiple block-sparse matrices are fused.

Evaluation and comparisons – From the previous set of experiments, we choose to focus our test using Full DeepPDNet with 6 layers and fusion of multiple block-sparse matrices “f5s2n10”, “f7s3n10” and “f14s7n10” as well as global projection “f28s28n10”. We evaluate the performance on the test set for five simulations considering different sizes of uniform blur (i.e. 3×3 , 5×5 and 7×7) with Gaussian noises of different standard deviation level (i.e $\alpha = 10, 20, 30$).

Our method is compared to unsupervised strategy when $g(L \cdot)$ models either a TV penalization or an NLTV penalization [57]. The algorithmic procedure to estimate \hat{x}_λ relies on the iterations described in Algorithm 1 when the error between two successive updates are less than 10^{-5} . We also compare to EPLL [18] which makes use of the Gaussian mixture model to learn the prior for image deblurring. Comparisons to supervised CNN-based procedure:

Method	Time (s)
EPLL [18]	1.27
TV [8]	0.07
NLTV [57]	0.19
MWCNN [58]	0.06
IRCNN [59]	0.66
Full DeepPDNet	0.01

Table 7: Average cost time (in s) per test image for MNIST dataset for different methods.

Data	Method	Blur filter 3×3			Blur filter 5×5		
		$\alpha = 15$ PSNR/SSIM	$\alpha = 25$ PSNR/SSIM	$\alpha = 50$ PSNR/SSIM	$\alpha = 15$ PSNR/SSIM	$\alpha = 25$ PSNR/SSIM	$\alpha = 50$ PSNR/SSIM
BSD68	TV [8]	25.52/0.6746	25.16/0.6634	23.27/0.5836	24.04/0.6141	23.83/0.6047	22.77/0.5622
	NLTV [57]	25.86/0.6875	25.49/0.6780	23.52/0.5932	24.22/0.6238	24.02/0.6165	22.88/0.5711
	EPLL [18]	27.01/0.7450	25.60/0.6785	23.72/0.6137	25.32/0.6674	24.38/0.6198	22.99/0.5715
	MWCNN [58]	26.56/0.7537	25.76/0.7136	23.88/0.6265	24.39/0.6533	24.03/0.6313	22.88/0.5759
	IRCNN [59]	26.78/0.7840	26.13/0.7203	23.63/0.5981	24.66/0.6947	24.64/0.6555	22.96/0.5651
	Full DeepPDNet (Q=28, K=6)	25.83/0.6628	24.63/0.6042	23.37/0.5789	24.44/0.6086	23.62/0.5612	22.27/0.5026
	Full DeepPDNet (Q=10, K=20)	27.33/0.7637	25.95/0.7055	23.69/0.6052	25.48/0.6819	24.66/0.6430	23.04/0.5717

Table 8: Comparison results of different methods on the BSD68 dataset from different degradation configurations.

MWCNN [58] and IRCNN [59] are also provided ¹. MWCNN integrates wavelet transform and inverse wavelet transform into U-Net architecture to contract the network and IRCNN employs a denoiser prior based on CNNs as a modular in the half quadratic splitting method for image restoration. The results on the test set are shown in Tab. 5. From the table, it is seen that the proposed DeepPDNet with Partial learning shows poor performance because of expressive ability limitation while full learning outperforms other methods significantly. We also give comparison results of average time cost per test image without using GPU for different methods in Tab. 7, it is observed that the proposed DeepPDNet is faster than other methods, which is certainly due to the simplicity and the small number of layers in our framework.

Figure 6 and Figure 9 respectively display the learned $L^{[k]}$ for the layer $k = 6$ on the MNIST and BSD400 dataset. In Figure 6 (a), we display the results when $L^{[k]}$ denotes a dense matrix. The illustration is composed of 100 small images corresponding to the $P = 100$ rows of $L^{[6]}$, each being reshaped as an image of size $\sqrt{N} \times \sqrt{N}$. Similarly, in Figure 6 (b), we display the learned rows of $L^{[k]}$ when the local-sparse matrix is considered $Q = 9$ and $P = 90$, leading to 90 small images of size $Q \times Q$. Similar information is displayed in Figures 9 (a) and (b) where both are associated with local-sparse $L^{[k]}$ but considering either a construction with $Q = 5$ (with the setting “f5s2n10”) or $Q = 7$ (with the setting “f7s3n10”).

Robustness to noise: We study the robustness of the proposed algorithm to additional

¹We download the source codes from the authors’ websites.

noise. We consider different level of Gaussian noise of standard deviation β to the test degraded images and forward them in the learned networks to obtain the restored ones. We evaluate the robustness for the learned models for different blur sizes: 3×3 , 5×5 , and 7×7 and Gaussian noise $\alpha = 20$. In Tab. 6, we show the performance of the restored images and the relative performance decrease ratio compared to the results without additional noise in Tab. 5. The results of MWCNN and IRCNN are also given in Tab. 6. It can be observed that: i) when the additional noise has a small variance, the performance drop for the proposed method is lower than the one with IRCNN; ii) the relative performance drop for MWCNN is lower than the one with the proposed Full DeepPDNet in most of scenarios, the possible reason is that wavelet transform is employed in the architecture to reduce the effect of additional noises; iii) when the additional noise is strong enough compared to the original noise, although serious performance drop occurs (for instance, 7×7 Blur when $\alpha = 20$ and $\beta = 20$) compared to MWCNN and IRCNN, the performance of our method are still better. To summarize, it is observed that the relative performance drop ratio of the proposed method is sometimes higher than the drop with IRCNN and MWCNN, however, the performance are still better than with these two state-of-the-art CNN-based methods. Finally, we visualize some instances of the restored images by MWCNN, IRCNN and Full DeepPDNet without/with additional noises in Fig. 7.

5.5 The performance on BSD68 dataset

In this section, we evaluate the performance of the proposed DeepPDNet² on the BSD68 dataset containing 68 natural images from Berkeley segmentation dataset with 500 images [53]. We follow [60] to use 400 images from BSD dataset of size 180×180 to train the network, and the 68 images are chosen from the BSD data for evaluation without the overlaps with the training set. In this work, we focus on the gray version of the BSD68 dataset for restoration. In the experiments, we take into account two different blur sizes (3×3 and 5×5) and three Gaussian noise levels ($\sigma = 15, 25, 50$). Few instances of the test images are displayed in Fig. 8.

Considering that test images in BSD68 dataset are of size 321×481 , it is particularly difficult to make \mathbf{z} be the whole image due to the huge memory demanding. We adopt a patch-based strategy that we train an affordable network by full learning from a collection of the patches of size $Q \times Q$ randomly extracted from training images with a number of about 200K, and then the learned network is traversed over a test image to obtain the deblurred image.

The comparison results with other methods are shown in Tab. 8. From the table, we can see that: i) due to a more complex dataset, the performance of different methods are worse than the ones on the MNIST dataset; ii) We first train a network of the same architecture

²Full DeepPDNet with filters “f5s2n20”+“f7s3n20”+“f14s7n20”+“f28s28n10”

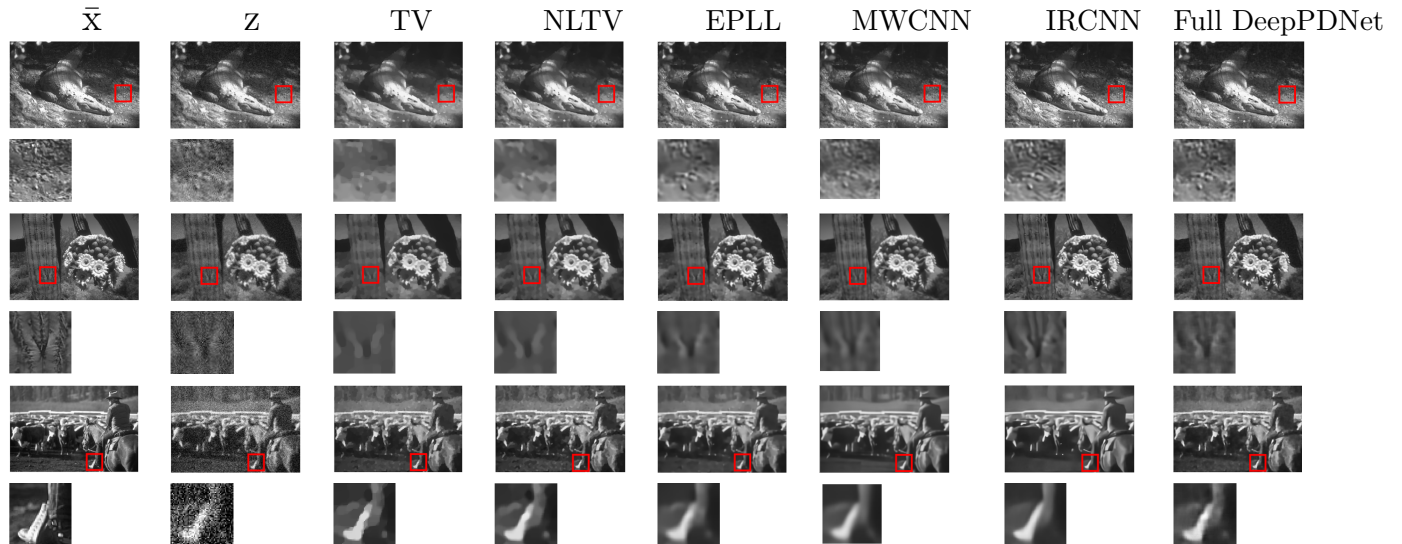


Figure 8: Visual comparisons on BSD68 dataset for different methods. The first row corresponds to the BSD68 data with a uniform 3×3 blur and a Gaussian noise with $\alpha = 15$, the second row is the zoomed regions of the red rectangles in the first row; the third row is with a uniform 5×5 blur and a Gaussian noise with $\alpha = 15$, the fourth row is the zoomed regions of the red rectangles in the third row; the fifth row is with a uniform 5×5 blur and a Gaussian noise with $\alpha = 50$, the sixth row is the zoomed regions of the red rectangles in the fifth row. For each instance, the images from the first to the seventh column respectively correspond to the original image \bar{x} , the degraded one z , the restored ones by TV, NLTV, EPLL, MWCNN, IRCNN and the proposed full DeepPDNet ($Q = 10, K = 20$).



Figure 9: Visualization of the non-zeros coefficients in $L^{[k]}$ for the layer $k = 6$ when considering Full DeepPDNet in the context of data degraded by a uniform 3×3 blur and an additive Gaussian noise with $\alpha = 20$ on BSD68 dataset. (a) Part of reshaped rows of the local sparse $L^{[6]}$ for the setting “f5s2n10” leading to $P = 1210$. (b) Part of reshaped rows of the local sparse $L^{[6]}$ for the setting “f7s3n10” leading to $P = 490$.

with the one used on the MNIST dataset, i.e. $Q = 28$, it is observed that the results are poor, especially for SSIM. We conjecture that the 6-layer network is not sufficient to express the complexity contents of the BSD dataset, therefore, we adopt a deeper network with 20 layer when $Q = 10$ which is easily affordable on the experimental platform, leading to a Full DeepPDNet with filters “f5s2n20”+“f7s3n20”+“f10s10n20”. We clearly observe that with deeper architecture, the performance are able to be further improved, especially for SSIM. Our proposed method obtains comparable results to MWCNN and IRCNN, which is based on a powerful deep convolutional network, allowing to capture the statistical property of the image; iii) the gap between different methods become less as the noise level becomes large. The instances of the deblurred images are shown in Fig. 8. The learned filters are shown in Fig. 9, we can see that the learned filters are meaningful to capture the local property.

5.6 Extension to Single Image Super-Resolution task

In this section, we investigate the adaptability of the proposed network on the single image super-resolution task. The goal of image super-resolution task is to generate a corresponding high-resolution (HR) image from a low-resolution (LR) image. Recently, the CNN-based deep networks have obtained promising performance by supervised learning. In the proposed method, in order to facilitate the modelization of A we restrict it to downsampling while state-of-the-art methods benefit from an input obtained from a bicubic interpolation. According to the results on BSD68 dataset in Section 5.5, the proposed network is a Full DeepPDNet with filters “f5s2n20”+“f7s3n20”+“f10s10n20” and $K = 20$. The learning stage is performed on the BSD200 dataset and is evaluated in the BSD100 and SET14 datasets used in [56] with downscaling factors 2, 3 and 4.

The performance comparisons are shown in Tab. 9. We compare the proposed algorithm with other CNN-based methods, for instance, SRCNN [61], VDSR [56], DnCNN [62], and MWCNN [58]³. SRCNN [61] directly learns an end-to-end mapping between the low/high resolution by using a deep CNN. Similar to VGG-net, VDSR [56] learns a very deep CNNs of 20 layers for accurate single-image super-resolution. DnCNN [62] adopts residual learning to predict the difference between the high-resolution ground truth and the bicubic upsampling of a low-resolution image, and MWCNN [58] integrates the wavelet transform to the U-Net architecture to obtain mid-level wavelet-CNN framework. We also propose to retrain MWCNN and DnCNN models, for which training codes are available. The training stage takes as an input z_s , obtained from a direct down-sampling, and the first layer of the network involves a direct upsampling of z_s . Similar procedure is considered for the test stage. From Table 9, it can be seen that: i) our method outperforms the released models of state-of-the-art methods; ii) for both re-trained MWCNN and DnCNN models, the performance are improved compared to their counterpart released models; iii) our method always outperforms the re-trained MWCNN for both BSD100 and SET14 datasets, iv) the performance of Full

³The test codes and released models are also downloaded from the authors’ websites.

Dataset	Method	Upscaling Factor		
		2	3	4
		PSNR/SSIM	PSNR/SSIM	PSNR/SSIM
BSD100	VDSR [56]	24.12/0.7242	21.09/0.5656	19.66/0.4896
	MWCNN [58]	23.66/0.6733	21.91/0.6078	21.38/0.5541
	DnCNN [62]	27.15/0.8089	22.12/0.6131	21.53/0.5803
	SRCNN [61]	26.63/0.7908	23.88/0.6469	22.42/0.5629
	Re-trained MWCNN [58]	28.59/0.8306	21.70/0.5987	22.32/0.5958
	Re-trained DnCNN [62]	27.25/0.8439	25.54/0.7315	23.99/0.6591
	Full DeepPDNet	28.88/0.8414	25.51/0.7155	23.93/0.6193
SET14	VDSR [56]	24.40/0.7528	20.71/0.5885	18.97/0.5042
	MWCNN [58]	22.93/0.6745	20.71/0.5801	19.52/0.5168
	DnCNN [62]	24.95/0.7653	22.27/0.6601	19.99/0.5518
	SRCNN [61]	25.65/0.7819	24.07/0.6906	21.12/0.5417
	Re-trained MWCNN [58]	28.78/0.8479	21.53/0.6201	21.64/0.6013
	Re-trained DnCNN [62]	29.07/0.8594	25.03/0.7568	24.51/0.6942
	Full DeepPDNet	28.58/0.8618	25.45/0.7453	23.17/0.6411

Table 9: Comparison results of different methods on the BSD100 and SET14 dataset for single image super-resolution task for different upscaling factors.

DeepPDNet and the re-trained DnCNN are comparable. Fig. 10 also visualizes the image instances by different methods.

6 Conclusion

This work aims to design a flexible network using prior knowledge on inverse problems both in terms of penalized co-log-likelihood design and optimization schemes. Our contribution is first to unfold the PDHG iterations and to establish a connection with standard neural networks with K layers. From this preliminary network, we design DeepPDNet that allows us to learn both the algorithmic step-size and the analysis linear operator (including implicitly the regularization parameter) involved in each layer. A full and a partial DeepPDNet are provided, one considering the learning of all the parameters without constraints leading to better numerical performance, and a second one allowing to provide a framework more adapted to theoretical stability analysis. Dense (i.e. global) or block-sparse (i.e. local) sparse analysis prior operators are considered. The backpropagation procedure is detailed. We employ the proposed network for two types of degradation: image deblur and single image super-resolution task, the experimental results illustrate that for images with small complexity such as MNIST, a network with few layers allows us to outperforms state-of-the-

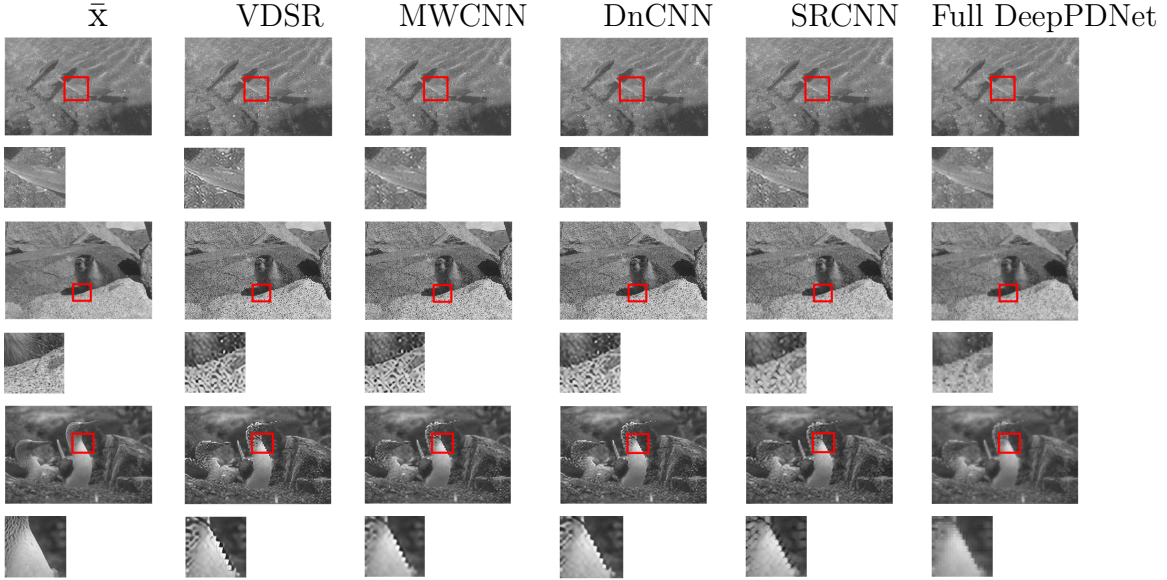


Figure 10: Visual comparisons on BSD100 dataset for different methods. The first row is the instances with 2 upscaling factor and the second row is the zoomed regions of the red rectangles in the first row; the third row is the instances with 3 upscaling factor and the fourth row is the zoomed regions of the red rectangles in the third row, the fifth row is the instances with 4 upscaling factor and the sixth row is the zoomed regions of the red rectangles in the fifth row.

art methods while for a more complex dataset, the proposed method outperforms standard unsupervised approaches such as TV, NLTV or EPLL and achieves comparable results with state-of-the-art CNN based methods. Moreover, we observed that the more complex is the dataset, the deeper needs to be the network.

Such a procedure can be extended to other type of degradation model considering for instance weighted data-term or by integrating only partial knowledge of degradation process in order to perform blind deconvolution following ideas provided in [45].

Appendix A: Computation of derivatives

1. $\frac{\partial u_s^{[k+1]}}{\partial c_s^{[k]}}$ is the derivative of output $u_s^{[k+1]}$ at layer $k+1$ w.r.t. $c_s^{[k]} = (c_{s,1}^{[k]}, c_{s,2}^{[k]})$ according to (12). Since identity acts on $c_{s,1}^{[k]}$ and proximity operator act on $c_{s,2}^{[k]}$, this yields to:

$$\frac{\partial u_s^{[k+1]}}{\partial c_s^{[k]}} = (u_1^\top, u_2^\top)^\top \in \mathbb{R}^N \times \mathbb{R}^P \quad (23)$$

where $\mathbf{u}_1 = (1, \dots, 1)$ and where $\mathbf{u}_{2,p}$ when $g = \|\cdot\|_1$ is:

$$\mathbf{u}_{2,p} = \begin{cases} 0 & \text{if } |c_{s,2,p}^{[k]}| > 1 \\ 1 & \text{if } |c_{s,2,p}^{[k]}| < 1 \\ [0, 1] & \text{if } c_{s,2,p}^{[k]} = \pm 1. \end{cases} \quad (24)$$

2. For the middle layers except the first and last layer, the derivative of the elementary of the network parameters $(D^{[k]}, b^{[k]})$ w.r.t. $\tau^{[k]}, \sigma^{[k]}, L^{[k]}$ (i.e. $\frac{\partial b_{[\ell]}^{[k]}}{\partial \tau_{[\ell]}^{[k]}}$, $\frac{\partial D_{[\ell]}^{[k]}}{\partial \tau_{[\ell]}^{[k]}}$, $\frac{\partial b_{[\ell]}^{[k]}}{\partial \sigma_{[\ell]}^{[k]}}$, $\frac{\partial D_{[\ell]}^{[k]}}{\partial \sigma_{[\ell]}^{[k]}}$, $\frac{\partial b_{[\ell]}^{[k]}}{\partial L_{[\ell]}^{[k]}}$ and $\frac{\partial D_{[\ell]}^{[k]}}{\partial L_{[\ell]}^{[k]}}$) can be easily obtained from Eq. (7):

$$\begin{cases} \frac{\partial b_{[\ell]}^{[k]}}{\partial \tau_{[\ell]}^{[k]}} = \begin{pmatrix} A^*z \\ 2\sigma_{[\ell]}^{[k]} L_{[\ell]}^{[k]} A^*z \end{pmatrix} \\ \frac{\partial D_{[\ell]}^{[k]}}{\partial \tau_{[\ell]}^{[k]}} = \begin{pmatrix} -A^*A & -L_{[\ell]}^{[k]*} \\ -2\sigma_{[\ell]}^{[k]} L_{[\ell]}^{[k]} A^*A & -2\sigma_{[\ell]}^{[k]} L_{[\ell]}^{[k]} L_{[\ell]}^{[k]*} \end{pmatrix} \\ \frac{\partial b_{[\ell]}^{[k]}}{\partial \sigma_{[\ell]}^{[k]}} = \begin{pmatrix} 0_{N \times 1} \\ 2\tau_{[\ell]}^{[k]} L_{[\ell]}^{[k]} A^*z \end{pmatrix} \\ \frac{\partial D_{[\ell]}^{[k]}}{\partial \sigma_{[\ell]}^{[k]}} = \begin{pmatrix} 0_{N \times N} & 0_{N \times P} \\ L_{[\ell]}^{[k]} (\text{Id} - 2\tau_{[\ell]}^{[k]} A^*A) & -2\tau_{[\ell]}^{[k]} L_{[\ell]}^{[k]} L_{[\ell]}^{[k]*} \end{pmatrix} \\ \frac{\partial b_{[\ell]}^{[k]}}{\partial L_{[\ell]}^{[k]}} = \begin{pmatrix} 0_{N \times 1} \\ 2\tau_{[\ell]}^{[k]} \sigma_{[\ell]}^{[k]} A^*z \end{pmatrix} \\ \frac{\partial D_{[\ell]}^{[k]}}{\partial L_{[\ell]}^{[k]}} = \begin{pmatrix} 0_{N \times N} & -\tau_{[\ell]}^{[k]} \\ \sigma_{[\ell]}^{[k]} (\text{Id} - 2\tau_{[\ell]}^{[k]} A^*A) & -4\tau_{[\ell]}^{[k]} \sigma_{[\ell]}^{[k]} L_{[\ell]}^{[k]*} \end{pmatrix} \end{cases} \quad (25)$$

and then the respective gradients are accumulated from all the elementary of the $D^{[k]}$, $b^{[k]}$. Similarly, the corresponding derivatives in the first and last layer are similarly calculated according to Eq. (9) and Eq. (25).

3. $\frac{\partial u_{s+1}^{[k]}}{\partial \sigma_{[\ell]}^{[k]}}$ is the gradient of conjugate of proximity operator ℓ_1 -norm w.r.t. $\sigma^{[k]}$ at iteration ℓ :

$$\frac{\partial u_s^{[k+1]}}{\partial \sigma_{[\ell]}^{[k]}} = 0. \quad (26)$$

Acknowledgement

This work is supported by the National Natural Science Foundation of China (61806180, U1804152), Key Research Projects of Henan Higher Education Institutions in China

(19A520037), Science and Technology Innovation Project of Zhengzhou (2019CXZX0037), and also by the ANR (Agence Nationale de la Recherche) of France (ANR-19-CE48-0009 Multisc’In).

References

- [1] A. Tikhonov, “Tikhonov regularization of incorrectly posed problems,” *Soviet Mathematics Doklady*, vol. 4, pp. 1624–1627, 1963.
- [2] S. Geman and D. Geman, “Stochastic relaxation, Gibbs distributions, and the Bayesian restoration of images,” in *Readings in Computer Vision*, pp. 564–584. Elsevier, 1987.
- [3] D. Mumford and J. Shah, “Optimal approximations by piecewise smooth functions and associated variational problems,” *Comm. Pure Applied Math.*, vol. 42, no. 5, pp. 577–685, 1989.
- [4] H. H. Bauschke and P. L. Combettes, *Convex analysis and monotone operator theory in Hilbert spaces*, Springer, New York, second edition, 2017.
- [5] P. L. Combettes and J.-C. Pesquet, “Proximal splitting methods in signal processing,” in *Fixed-Point Algorithms for Inverse Problems in Science and Engineering*, H. H. Bauschke, R. S. Burachik, P. L. Combettes, V. Elser, D. R. Luke, and H. Wolkowicz, Eds., pp. 185–212. Springer-Verlag, New York, 2011.
- [6] Y. LeCun, Y. Bengio, and G. Hinton, “Deep learning,” *Nature*, vol. 521, no. 7553, pp. 436–444, 2015.
- [7] P. Charbonnier, L. Blanc-Féraud, G. Aubert, and M. Barlaud, “Deterministic edge-preserving regularization in computed imaging,” *IEEE Transactions on Image Processing*, vol. 6, no. 2, pp. 298–311, 1997.
- [8] L. Rudin, S. Osher, and E. Fatemi, “Nonlinear total variation based noise removal algorithms,” *Phys. D Nonlinear Phenomena*, vol. 60, no. 1, pp. 259–268, 1992.
- [9] L. I Rudin and S. Osher, “Total variation based image restoration with free local constraints,” in *Image Processing, 1994. Proceedings. ICIP-94., IEEE International Conference. IEEE*, 1994, vol. 1, pp. 31–35.
- [10] A. Chambolle and P.-L. Lions, “Image recovery via total variation minimization and related problems,” *Numerische Mathematik*, vol. 76, no. 2, pp. 167–188, 1997.
- [11] A. Chambolle, “An algorithm for total variation minimization and applications,” *Journal of Mathematical imaging and vision*, vol. 20, no. 1-2, pp. 89–97, 2004.

- [12] S. Osher, M. Burger, D. Goldfarb, J. Xu, and W. Yin, “An iterative regularization method for total variation-based image restoration,” *Multiscale Modeling & Simulation*, vol. 4, no. 2, pp. 460–489, 2005.
- [13] L. Condat, “Discrete total variation: New definition and minimization,” *SIAM J. Imaging Sci.*, vol. 10, no. 3, pp. 1258–1290, 2017.
- [14] G. Peyré, S. Bougleux, and L. Cohen, “Non-local regularization of inverse problems,” in *European Conference on Computer Vision*. Springer, 2008, pp. 57–68.
- [15] Z. Li, F. Malgouyres, and T. Zeng, “Regularized non-local total variation and application in image restoration,” *J. Math. Imag. Vis.*, vol. 59, no. 2, pp. 296–317, 2017.
- [16] M. Elad, P. Milanfar, and R. Ron, “Analysis versus synthesis in signal priors,” *Inverse Problems*, vol. 23, no. 3, pp. 947–968, 2007.
- [17] L. Chaâri, N. Pustelnik, C. Chaux, and J.-C. Pesquet, “Solving inverse problems with over-complete transforms and convex optimization techniques,” in *Proc. SPIE, Wavelets XIII*, San Diego, California, USA, Aug. 2-8 2009, vol. 7446, p. 14p.
- [18] D. Zoran and Y. Weiss, “From learning models of natural image patches to whole image restoration,” in *Proc. IEEE Int. Conf. Comput. Vis.*, Barcelona, Spain, Nov. 6-13 2011, pp. 479–486.
- [19] A. Danielyan, V. Katkovnik, and K. Egiazarian, “BM3D frames and variational image deblurring,” *IEEE Trans. Image Process.*, vol. 21, no. 4, pp. 1715–1728, 2012.
- [20] N. Pustelnik, A. Benazza-Benhayia, Y. Zheng, and J.-C. Pesquet, “Wavelet-based image deconvolution and reconstruction,” *Wiley Encyclopedia of EEE*, 2016.
- [21] L. Condat, D. Kitahara, A. Contreras, and A. Hirabayashi, “Proximal splitting algorithms: Relax them all!,” *arXiv:1912.00137*, 2019.
- [22] P. L. Combettes and V. R. Wajs, “Signal recovery by proximal forward-backward splitting,” *Multiscale Modeling & Simulation*, vol. 4, no. 4, pp. 1168–1200, 2005.
- [23] A. Beck and M. Teboulle, “A fast iterative shrinkage-thresholding algorithm for linear inverse problems,” *SIAM Journal on Imaging Sciences*, vol. 2, no. 1, pp. 183–202, 2009.
- [24] A. Chambolle and C. Dossal, “On the convergence of the iterates of the Fast Iterative Shrinkage/Thresholding Algorithm,” *Journal of Optimization Theory and Applications*, vol. 166, no. 3, pp. 968–982, Sep. 2015.
- [25] P. L. Combettes and J.-C. Pesquet, “A Douglas-Rachford splitting approach to nonsmooth convex variational signal recovery,” *IEEE Journal of Selected Topics in Signal Processing*, vol. 1, no. 4, pp. 564–574, 2007.

- [26] S. Setzer, *Split Bregman algorithm, Douglas-Rachford splitting and frame shrinkage*, vol. 5567, chapter Scale Space and Variational Methods in Computer Vision. SSVM 2009. Lecture Notes in Computer Science, pp. 464–476, 2009.
- [27] L. Condat, “A primal-dual splitting method for convex optimization involving lipschitzian, proximable and linear composite terms,” *J. Optim. Theory Appl.*, vol. 158, no. 2, pp. 460–479, 2013.
- [28] B. C. Vũ, “A splitting algorithm for dual monotone inclusions involving cocoercive operators,” *Advances in Computational Mathematics*, vol. 38, no. 3, pp. 667–681, Apr. 2013.
- [29] R. Ammanouil, A. Ferrari, D. Mary, C. Ferrari, and F. Loi, “A parallel and automatically tuned algorithm for multispectral image deconvolution,” *Monthly Notices of the Royal Astronomical Society*, vol. 490, no. 1, pp. 37–49, August 2019.
- [30] B. Pascal, S. Vaiteer, N. Pustelnik, and P. Abry, “Automated data-driven selection of the hyperparameters for total-variation based texture segmentation,” *arXiv:2004.09434*, 2020.
- [31] S. Ramani, T. Blu, and M. Unser, “Monte-carlo SURE: A black-box optimization of regularization parameters for general denoising algorithms,” *IEEE Trans. Image Process.*, vol. 17, no. 9, pp. 1540–1554, 2008.
- [32] Y. C Eldar, “Generalized SURE for exponential families: Applications to regularization,” *IEEE Trans. Signal Process.*, vol. 57, no. 2, pp. 471–481, 2008.
- [33] J.-C. Pesquet, A. Benazza-Benyahia, and C. Chaux, “A SURE approach for digital signal/image deconvolution problems,” *IEEE Trans. Signal Process.*, vol. 57, no. 12, pp. 4616–4632, 2009.
- [34] C.-A. Deledalle, S. Vaiteer, J. Fadili, and G. Peyré, “Stein unbiased gradient estimator of the risk (sugar) for multiple parameter selection,” *SIAM J. Imaging Sci.*, vol. 7, no. 4, pp. 2448–2487, 2014.
- [35] A. Lucas, M. Iliadis, R. Molina, and A.K. Katsaggelos, “Using deep neural networks for inverse problems in imaging: Beyond analytical methods,” *IEEE Signal Processing Magazine*, vol. 35, no. 1, pp. 20–36, Jan. 2018.
- [36] S. Ravishankar, J.C. Ye, and J.A. Fessler, “Deep convolutional framelets: A general deep learning framework for inverse problems,” *arXiv:1904.02816s*, 2019.
- [37] X.-J. Mao, C. Shen, and Y.-B. Yang, “Using deep neural networks for inverse problems in imaging: Beyond analytical methods,” *Advances in Neural Information Processing Systems*, vol. 29, Dec. 5-10 2016.

- [38] D. Ulyanov, A. Vedaldi, and V. Lempitsky, “Deep image prior,” *International Journal of Computer Vision*, vol. 128, pp. 1867–1888, Oct. 2020.
- [39] L. Xu, J.S.J. Ren, C. Liu, and J. Jia, “Deep convolutional neural network for image deconvolution,” in *Proc. Advances in Neural Information Processing Systems*, Montréal, Canada, Dec. 8-13 2014, vol. 27.
- [40] E. Kang, J. Min, and J.C. Ye, “A deep convolutional neural network using directional wavelets for low-dose X-ray CT reconstruction,” *Med Phys.*, vol. 44, no. 10, pp. 360–375, Oct. 2017.
- [41] J.C. Ye, Y. Han, and E. Cha, “Deep convolutional framelets: A general deep learning framework for inverse problems,” *SIAM Journal on Imaging Sciences*, vol. 11, no. 2, pp. 991–1048, 2018.
- [42] T. A. Bubba, G. Kutyniok, M. Lassas, M. M’arz, W. Samek, S. Siltanen, and V. Srinivasan, “Learning the invisible: A hybrid deep learning-shearlet framework for limited angle computed tomography,” *Inverse Problems*, vol. 35, 2019.
- [43] K. H. Jin, M. T. McCann, E. Froustey, and M. Unser, “Deep Convolutional Neural Network for inverse problems in imaging,” *IEEE Trans. Image Process.*, vol. 26, no. 9, pp. 4509–4522, Jun. 2017.
- [44] D. Gilton, G. Ongie, and R. Willett, “Neumann networks for linear inverse problems in imaging,” *IEEE Transactions on Computational Imaging*, vol. 9, pp. 328–343, 2019.
- [45] D. Ren, W. Zuo, D. Zhang, L. Zhang, and M. Yang, “Simultaneous fidelity and regularization learning for image restoration,” *IEEE Transactions on Pattern Analysis and Machine Intelligence*, pp. 1–1, 2019.
- [46] K. Gregor and Y. LeCun, “Learning fast approximations of sparse coding,” in *Proc. International Conference on Machine Learning*, Haifa, Israel, Jun. 21-24 2010, pp. 399–406.
- [47] C. Bertocchi, E. Chouzenoux, M.-C. Corbineau, J.-C. Pesquet, and M. Prato, “Deep unfolding of a proximal interior point method for image restoration,” *Inverse Problems*, vol. 36, no. 3, pp. 034005, feb 2020.
- [48] J. Adler and O. Oktem, “Learned primal-dual reconstruction,” *IEEE Trans. Med. Imag.*, vol. 37, no. 6, pp. 1322–1332, 2018.
- [49] K. Zhang, W. Zuo, S. Gu, and L. Zhang, “Learning deep CNN denoiser prior for image restoration,” in *IEEE Conference on Computer Vision and Pattern Recognition*, Jul. 21-26 2017, pp. 3929–3938.
- [50] P. Combettes and J.-C. Pesquet, “Deep neural network structures solving variational inequalities,” *Set-Valued and Variational Analysis*, 2020.

- [51] J. Boulanger, N. Pustelnik, L. Condat, L. Sengmanivong, and T. Piolot, “Nonsmooth convex optimization for structured illumination microscopy image reconstruction,” *Inverse Problems*, vol. 34, no. 9, 2018.
- [52] Y LeCun, L Botto, Y Bengio, and P Haffner, “Gradient-based learning applied to document recognition,” *Proceedings of IEEE*, vol. 86, no. 11, pp. 2278–2324, 1998.
- [53] S. Roth and M. J. Black, “Fields of experts,” *International Journal of Computer Vision*, vol. 82, no. 2, pp. p.205–229, 2009.
- [54] R. Timofte, V. De Smet, and L. Van Gool, “A+: Adjusted anchored neighborhood regression for fast super-resolution,” 2014, Springer.
- [55] R. Reyde, M. Elad, and M. Protter, “On single image scale-up using sparse-representations,” *Curves and Surfaces*, pp. 711–730, 2012.
- [56] J. Kim, J. Lee, and K. Lee, “Accurate image super-resolution using very deep convolutional networks,” in *2016 IEEE Conference on Computer Vision and Pattern Recognition (CVPR)*, Los Alamitos, CA, USA, jun 2016, pp. 1646–1654.
- [57] G. Chierchia, N. Pustelnik, B. Pesquet-Popescu, and J.-C. Pesquet, “A nonlocal structure tensor-based approach for multicomponent image recovery problems,” *IEEE Trans. Image Process.*, vol. 23, pp. 5531–5544, 2014.
- [58] P. Liu, H. Zhang, K. Zhang, L. Lin, and W. Zuo, “Multi-level wavelet-CNN for image restoration,” in *2018 IEEE/CVF Conference on Computer Vision and Pattern Recognition Workshops (CVPRW)*, Los Alamitos, CA, USA, jun 2018, pp. 886–88609, IEEE Computer Society.
- [59] K. Zhang, W. Zuo, S. Gu, and L. Zhang, “Learning deep cnn denoiser prior for image restoration,” in *2017 IEEE Conference on Computer Vision and Pattern Recognition (CVPR)*, 2017, pp. 2808–2817.
- [60] Y. Chen and T. Pock, “Trainable nonlinear reaction diffusion: A flexible framework for fast and effective image restoration,” *IEEE Trans. Pattern Anal. Match. Int.*, vol. 39, no. 6, pp. 1256–1272, 2017.
- [61] C. Dong, C. L. Chen, K. He, and X. Tang, “Learning a deep convolutional network for image super-resolution,” in *ECCV. 2014*, pp. 184–199, Springer International Publishing.
- [62] K. Zhang, W. Zuo, Y. Chen, D. Meng, and L. Zhang, “Beyond a Gaussian denoiser: Residual learning of deep CNN for image denoising,” *IEEE Trans. Image Process.*, vol. 26, no. 7, pp. 3142–3155, 2017.